

*Carnegie Supernova Project-II: Using Near-Infrared Spectroscopy to determine the location of the outer ⁵⁶Ni in Type Ia Supernovae**

C. ASHALL,¹ E. Y. HSIAO,¹ P. HOEFLICH,¹ M. STRITZINGER,² M. M. PHILLIPS,^{1,3} N. MORRELL,³ S. DAVIS,¹ E. BARON,^{2,4,5}
A. L. PIRO,⁶ C. BURNS,⁶ C. CONTRERAS,⁷ L. GALBANY,⁸ S. HOLMBO,² R. P. KIRSHNER,^{9,10} K. KRISCIUNAS,¹¹
G. H. MARION,¹² D. J. SAND,¹³ M. SHAHBANDEH,¹ N. B. SUNTZEFF,¹⁴ AND F. TADDIA^{2,15}

¹*Department of Physics, Florida State University, Tallahassee, FL 32306, USA*

²*Department of Physics and Astronomy, Aarhus University, Ny Munkegade 120, DK-8000 Aarhus C, Denmark*

³*Carnegie Observatories, Las Campanas Observatory, 601 Casilla, La Serena, Chile*

⁴*Homer L. Dodge Department of Physics and Astronomy, University of Oklahoma, 440 W. Brooks, Rm 100, Norman, OK 73019-2061, USA*

⁵*Hamburger Sternwarte, Gojenbergsweg 112, D-21029 Hamburg, Germany*

⁶*Observatories of the Carnegie Institution for Science, 813 Santa Barbara St., Pasadena, CA 91101, USA*

⁷*Carnegie Observatories, Las Campanas Observatory, 601 Casilla, La Serena, Chile*

⁸*PITT PACC, Department of Physics and Astronomy, University of Pittsburgh, Pittsburgh, PA 15260, USA*

⁹*Gordon and Betty Moore Foundation, 1661 Page Mill Road, Palo Alto, CA 94304*

¹⁰*Harvard-Smithsonian Center for Astrophysics, 60 Garden Street, Cambridge, MA 02138*

¹¹*George P. and Cynthia Woods Mitchell Institute for Fundamental Physics & Astronomy, Texas A&M University, Department of Physics, 4242 TAMU, College Station, TX 77843*

¹²*University of Texas at Austin, 1 University Station C1400, Austin, TX, 78712-0259, USA*

¹³*Department of Astronomy/Steward Observatory, 933 North Cherry Avenue, Rm. N204, Tucson, AZ 85721-0065, USA*

¹⁴*George P. and Cynthia Woods Mitchell Institute for Fundamental Physics & Astronomy, Texas A&M University, Department of Physics and Astronomy, 4242 TAMU, College Station, TX 77843*

¹⁵*The Oskar Klein Centre, Department of Astronomy, Stockholm University, AlbaNova, 106 91 Stockholm, Sweden*

(Received April 8, 2019; Revised; Accepted)

Submitted to ApJL

ABSTRACT

We present the H -band wavelength region of thirty-seven post-maximum light near-infrared (NIR) spectra of three normal, nine transitional and four sub-luminous type Ia supernovae (SNe Ia), extending from +5 d to +20 d relative to the epoch of B -band maximum. We introduce a new observable, the blue-edge velocity, v_{edge} , of the prominent Fe/Co/Ni-peak H -band emission feature which is quantitatively measured. The v_{edge} parameter is found to decrease over sub-type ranging from around $-14,000$ km s⁻¹ for normal SNe Ia, to $-10,000$ km s⁻¹ for transitional SNe Ia, down to $-5,000$ km s⁻¹ for the sub-luminous SNe Ia. Furthermore, inspection of the $+10 \pm 3$ d spectra indicates that v_{edge} is correlated with the color-stretch parameter, s_{BV} , and hence with peak luminosity. These results follow the previous findings that brighter SNe Ia tend to have ⁵⁶Ni located at higher velocities as compared to sub-luminous objects. As v_{edge} is a model-independent parameter, we propose it can be used in combination with traditional observational diagnostics to provide a new avenue to robustly distinguish between leading SNe Ia explosion models.

Keywords: supernovae: general

1. INTRODUCTION

Type Ia supernovae (SNe Ia) are the thermonuclear explosions of at least one carbon-oxygen white dwarf (WD) in a binary system. However the exact nature of

Corresponding author: Chris Ashall
Chris.Ashall@gmail.com

* This paper includes data gathered with the 6.5 meter Magellan Telescopes located at Las Campanas Observatory, Chile

their progenitors and critical details of their explosion physics remain open questions.

The currently favoured progenitor scenarios are the single degenerate scenario (SDS), where a WD accretes material from a non-degenerate companion star such as a H/He or red giant star (Whelan & Iben 1973; Livne 1990), and the double degenerate scenario (DDS), consisting of two WDs (Iben & Tutukov 1984). Within each progenitor scenario there are different explosion mechanisms, and progenitor masses. However, it is still not clear if all of these scenarios are seen in nature, and if one of them dominates the production of SNe Ia in the Universe. For a recent review on SNe Ia explosion scenarios see Livio & Mazzali (2018).

SNe Ia follow a luminosity-width-relation (LWR), where brighter objects have broader light curves (Phillips 1993). Sub-luminous, 1991bg-like (Filippenko et al. 1992) SNe Ia are located at the faint end of the LWR (e.g., Ashall et al. 2016a), and depending on the parameter combination used, sub-luminous SNe Ia have been proposed to be both part of a continuous distribution from normal SNe Ia (e.g., Hoefflich et al. 2017; Ashall et al. 2018; Burns et al. 2018), and from a distinct population (e.g., Stritzinger et al. 2006; Dhawan et al. 2017; Blondin et al. 2017; Scalzo et al. 2019).

At NIR wavelengths SNe Ia are nearly standard candles and suffer from less systematic effects compared to the optical (Krisciunas et al. 2004a; Wood-Vasey et al. 2008; Mandel et al. 2011; Kattner et al. 2012; Burns et al. 2014; Dhawan et al. 2018; Avelino et al. 2019). As a result current SNe Ia cosmology programs such as the *Carnegie Supernova Project II* (CSP-II; Phillips et al. 2019) have turned their attention towards longer wavelengths.

NIR spectroscopy offers a promising way to investigate the physics of SNe Ia, as it enable us to receive light from different depths in a supernova’s atmosphere at the same epoch. This means a single NIR spectrum can simultaneously probe different burning regions in a SN Ia explosion. For normal bright SNe Ia in the NIR, by a few days past maximum light¹, there is no well-defined photosphere, and line blanketing dominates the opacity. In the region where there are lines, this opacity provides a quasi-continuum which is formed at relatively large radii. Conversely, in areas with few lines there is less opacity, enabling much deeper regions of the ejecta to be visible.

One wavelength region of interest coincides with the *H*-band where, between maximum light and +10 d, a

complex iron-peak emission feature emerges due to allowed transitions located above the photosphere (Kirshner et al. 1973; Wheeler et al. 1998; Höflich et al. 2002; Marion et al. 2009; Hsiao et al. 2013). Previous work has found a correlation between the strength of this feature and the color-stretch parameter (Hsiao et al. 2013). Moreover, with a limited sample, Hsiao (2009) found an indication of a correlation between the velocity of this feature and light curve shape. This iron-peak feature consists of a blend of many Fe II/Co II/Ni II allowed emission lines. The Fe and Co in these epochs are produced through the radioactive decay of ⁵⁶Ni. To first order, the luminosity of a supernova is dependent on the amount of ⁵⁶Ni synthesized in the explosion, where less luminous objects produce smaller amounts of ⁵⁶Ni (e.g., Arnett 1982; Stritzinger et al. 2006; Mazzali et al. 2007).

A primary objective of the CSP-II was to obtain a large sample of NIR spectra of SN Ia (Hsiao et al. 2019). In this work, we use a subset of these spectra to examine the *H*-band iron-peak feature in transitional and sub-luminous SNe Ia. Transitional objects are a link between normal-bright SNe Ia and the sub-luminous, 1991bg-like population (see e.g., Pastorello et al. 2007; Hsiao et al. 2015; Ashall et al. 2016a,b; Gall et al. 2018). Transitional SNe Ia are characterized by having: i) fast declining light curves, with $\Delta m_{15}(B) > 1.6$ mag, ii) a secondary *i*-band NIR maxima which peaks after the time of *B*-band maximum, iii) and no strong Ti II absorption at 4400Å.

Here, we suggest that the highest blue-edge velocity (v_{edge}) of the iron-peak feature represents the outer edge of ⁵⁶Ni in the SNe Ia explosion. In an accompanying paper (Ashall et al. 2019) we compare v_{edge} to explosion models, and demonstrate it is a measurement of the specific kinetic energy in SNe Ia. We also show that v_{edge} is a quantification of the outer ⁵⁶Ni abundance in the ejecta. v_{edge} measures the point in velocity space where X_{Ni} falls to of order 0.03-0.10. Therefore, v_{edge} is a direct probe of the sharp transition between the incomplete and complete Si-burning regions in the ejecta.

Finally, we note that although the light-curve decline-rate parameter – $\Delta m_{15}(B)$ ² – has successfully been used to calibrate the luminosity of SNe Ia, it is degenerate when dealing with sub-luminous and transitional objects. This is because, for the least luminous SNe Ia, the inflection point in the *B*-band light curve occurs prior to +15 d (Phillips 2012). Therefore, throughout the following work we characterize the properties of SNe Ia light

¹ Throughout this paper phases (in days) are given with respect to time of rest frame *B*-band maximum.

² $\Delta m_{15}(B)$ is the difference in magnitude between maximum light and +15 d (Phillips 1993).

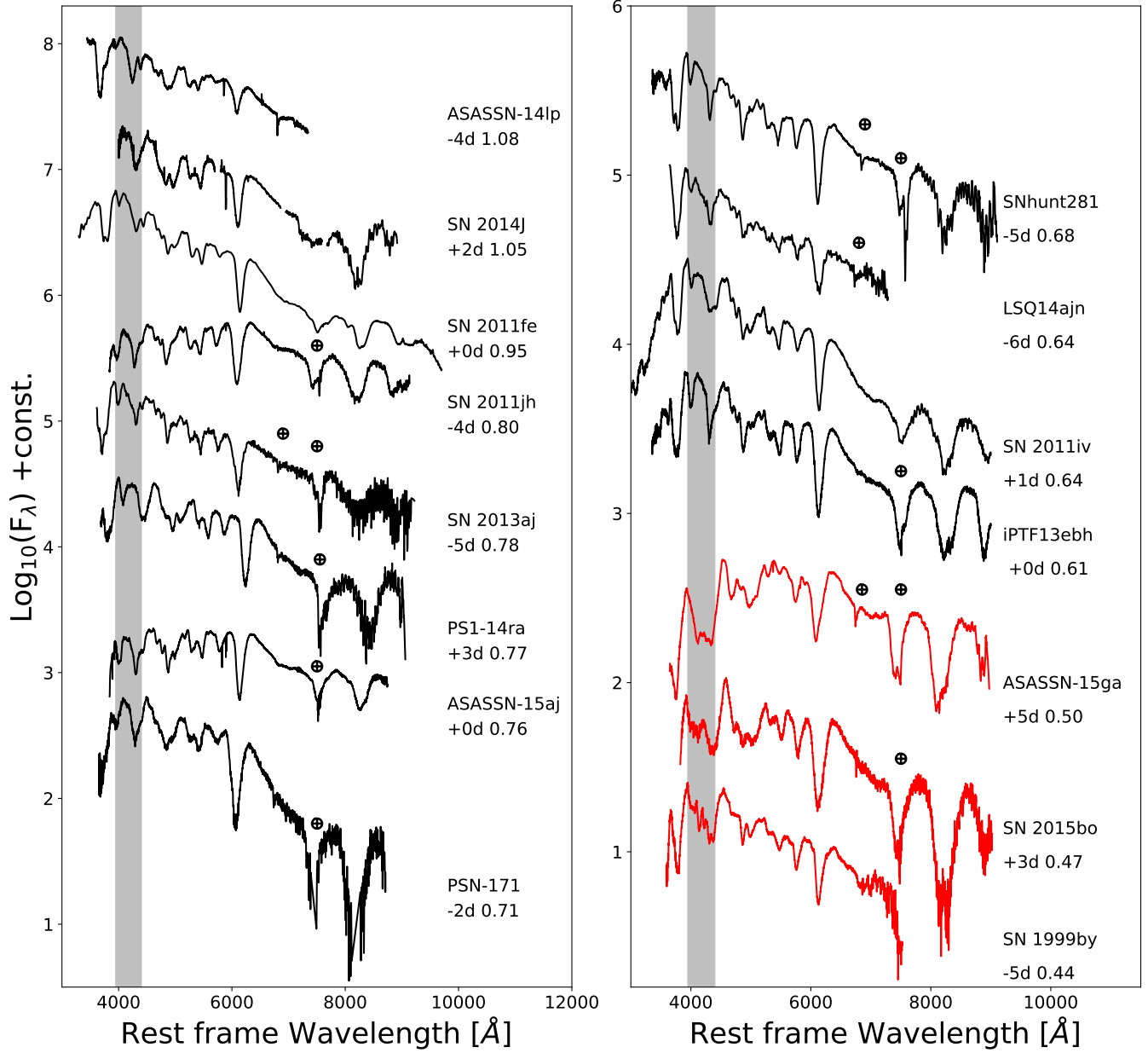


Figure 1. Rest-frame visual-wavelength spectra of the SNe used in this work. Their phase relative to maximum and as well as s_{BV} is plotted adjacent to each spectrum. The objects are plotted in order of s_{BV} , and those in red have strong Ti II absorption at 4400\AA . The grey vertical region highlights the Ti II 4400\AA feature. All of the spectra are from N. Morrell et al. in prep., except for, ASASSN-14lp (Shappee et al. 2016), SN 2014J (Ashall et al. 2014), SN 2011fe (Pereira et al. 2013), SN 2011iv (Gall et al. 2018), iPTF13ebh (Hsiao et al. 2015), SN 1999by (Garnavich et al. 2004), and SN 2014ah (Yaron & Gal-Yam 2012). The telluric features in the spectra are marked.

curves with the color-stretch s_{BV} parameter. s_{BV} is a dimensionless parameter defined as the time difference between B -band maximum and the reddest point in the $B - V$ color curve divided by 30 days, where typical SNe Ia have $s_{BV} \approx 1$ (Burns et al. 2014).

2. OBSERVATIONAL SAMPLE

The selection criteria for the sample were set such that the SNe Ia were transitional or sub-luminous (i.e., they had $s_{BV} < 0.8$), and have at least one NIR spectrum, between +5 and +20 d, as these are the phases when it is predicted that the Fe/Co/Ni emission occurs (Marion et al. 2009), and is when the H -band break appears in the spectroscopic data. There were 12 SNe Ia that met these criteria from the CSP-II data set. The sub-luminous

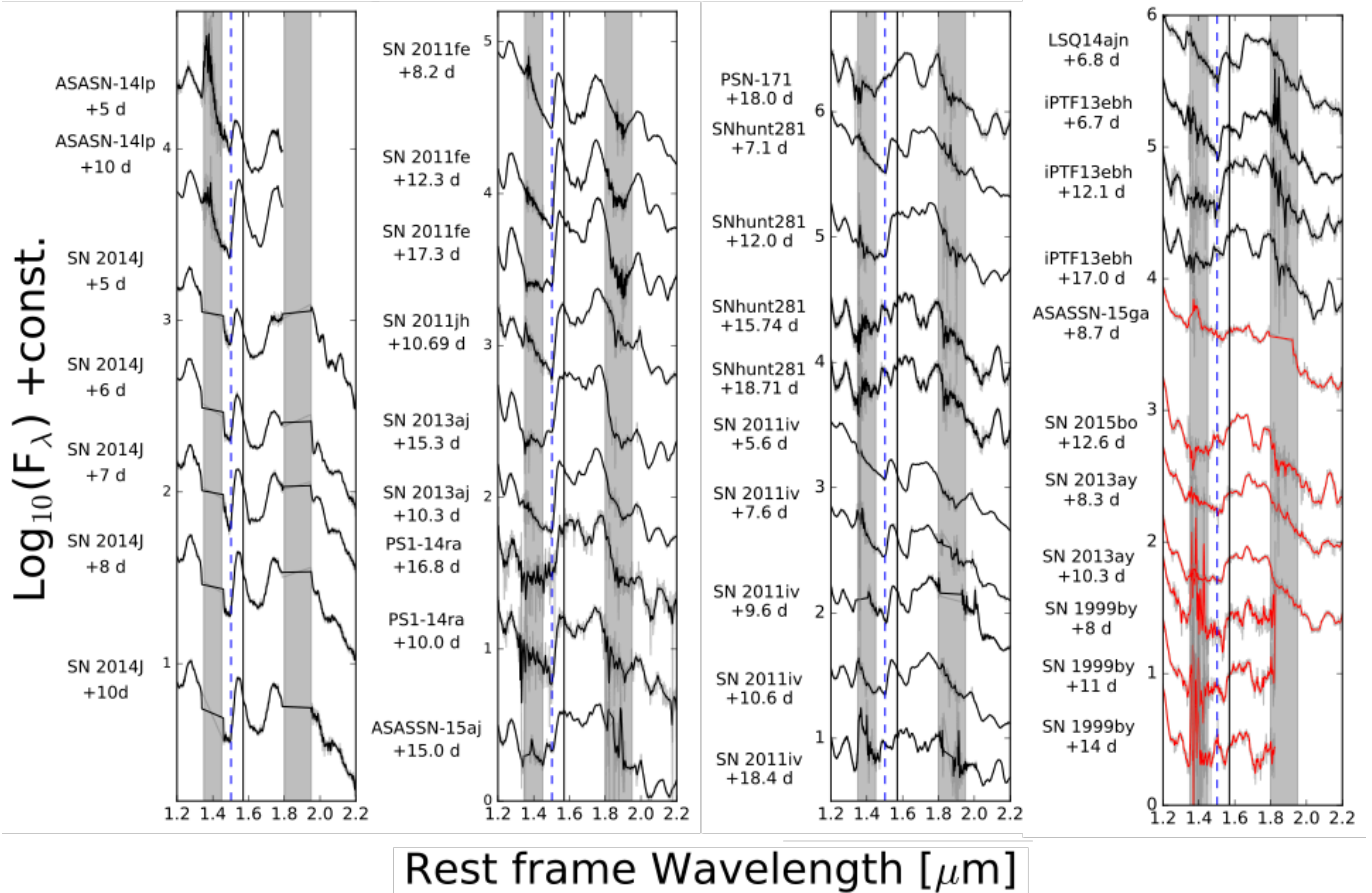


Figure 2. The CSP-II SNe Ia NIR spectra used in this paper, sorted by s_{BV} , where the objects get fainter from going from the top of the left panel to the bottom of the right panel. The name of each supernova and its time relative to B -band maximum is adjacent to each spectrum. The Gaussian smoothed ($\sigma=2$) spectra are plotted in black and red and the un-smoothed spectra are underneath in grey. The vertical grey regions are the telluric bands in the NIR. The vertical black lines denote the rest wavelength of the $1.57\mu\text{m}$ feature, and the dashed blue line corresponds to the same feature at $-13,000\text{km s}^{-1}$.

SN 1999by ($s_{BV}=0.44$) (Höflich et al. 2002) and the normal SN 2011fe ($s_{BV}=0.95$), SN 2014J ($s_{BV}=1.05$), and ASASSN-14lp ($s_{BV}=1.084$) (Pereira et al. 2013; Hsiao et al. 2013; Marion et al. 2015) were also used in the analysis. The basic properties of these SNe are presented in Table 1.

Optical spectra near maximum light of our sample (eight of which are unpublished) are plotted in Fig. 1. A summary of the optical spectra can be found in Table 1. The three SNe Ia plotted in red show the typical characteristic of sub-luminous SNe Ia, a strong Ti II absorption feature at $\sim 4400\text{\AA}$. The other SNe Ia have a higher ionization state and are classical transitional objects, except for SN 2011fe, SN 2014J and ASASSN-14lp which are normal-bright SNe Ia. We note that SN 2013ay was classified from a NIR spectrum (Hsiao et al. 2013), has a light curve shape consistent with a sub-luminous SNe Ia and an $s_{BV}=0.46\pm 0.05$, but does not have optical spectra. The unpublished CSP-II photometry of all the supernovae was checked, and the SNe

Ia that were spectroscopically sub-luminous events were found to have small, but not barely visible, secondary i -band maximum. Due to a lack of pre-maximum light curve coverage, for the sub-luminous SNe Ia it was not possible to determine the i -band maximum relative to the B -band, except for SN 2015bo which peaked in the i band before the B -band.

There are 37 NIR spectra of the 16 SNe Ia in the sample, 18 of which are unpublished (see Table 1 for details). Most of the spectra were observed with the FIRE spectrograph on the Magellan Baade telescope at Las Campanas Observatory, the other unpublished spectra were observed with SpeX on the NASA Infrared Telescope Facility (IRTF), Gemini Near-Infrared Spectrograph (GNIRS) on Gemini-North, and FLAMINGOS-2 on Gemini-South. The spectra were reduced and corrected for telluric features via the procedure described by Hsiao et al. (2019).

The full sample of the NIR spectra is plotted in Fig. 2. Each spectrum is corrected to the rest-frame, labeled

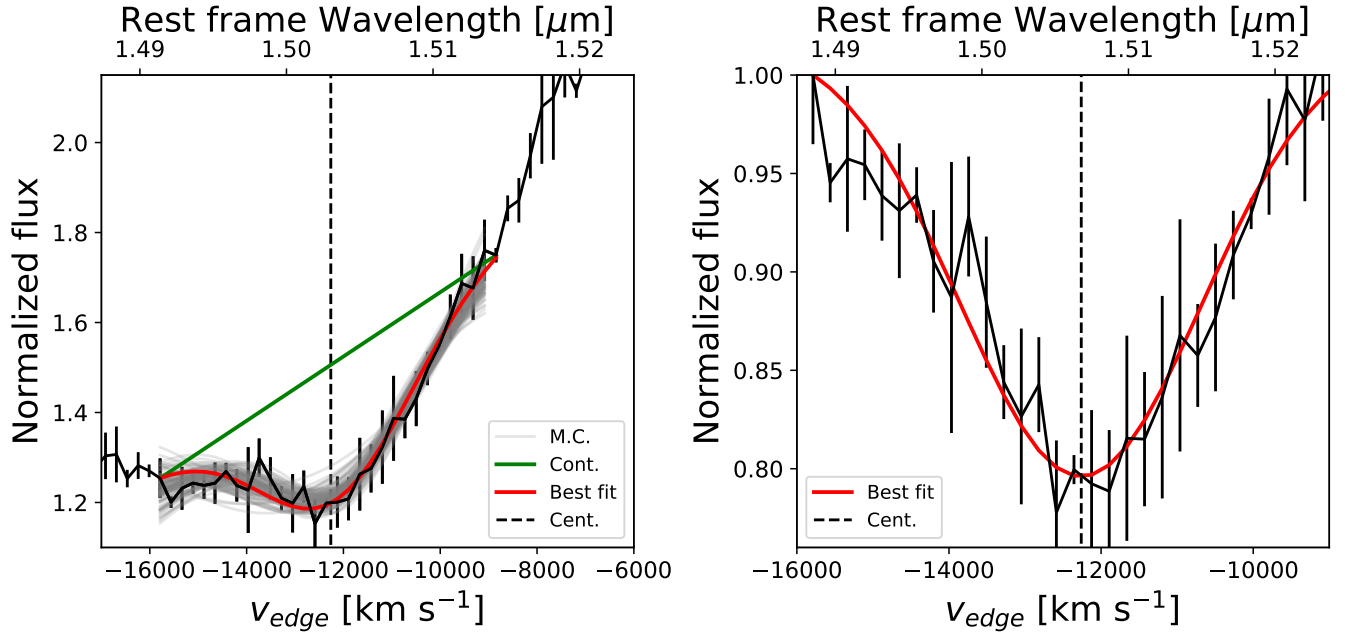


Figure 3. An example of how v_{edge} is determined using the +7.09 d spectrum of SNhunt281. *Left:* The continuum (green) determined from iteration from the Gaussian fit, the best Gaussian fit (red), the data (black solid), the central value of the Gaussian (black dashed), and the 100 Monte Carlo realizations (grey). The flux errors of the observations are provided as error bars. *Right:* The best Gaussian fit (red), the normalized data (black solid), and the central value of the Gaussian (black dashed) produced through the fitting process. The continuum from the left panel has been removed.

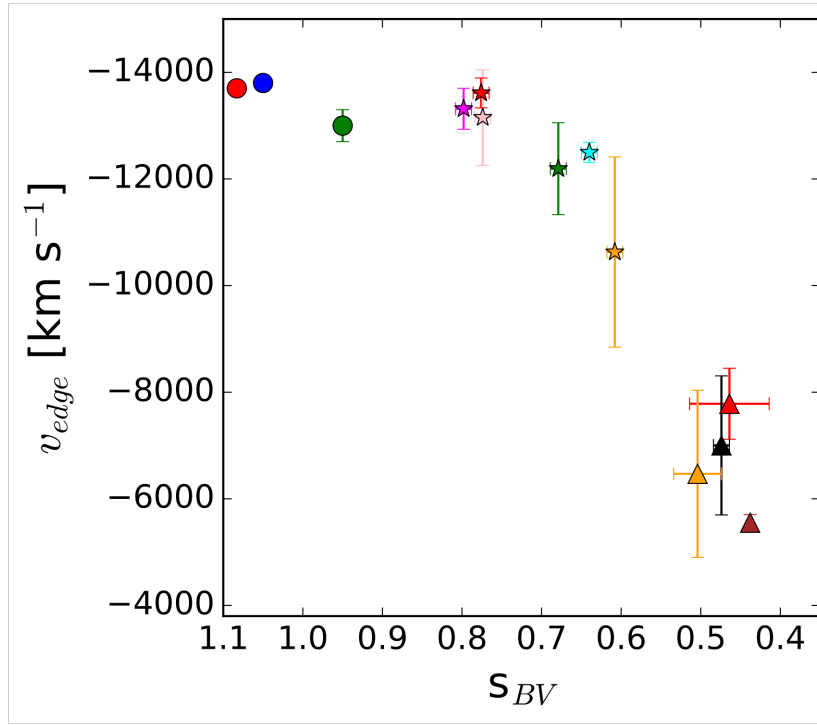
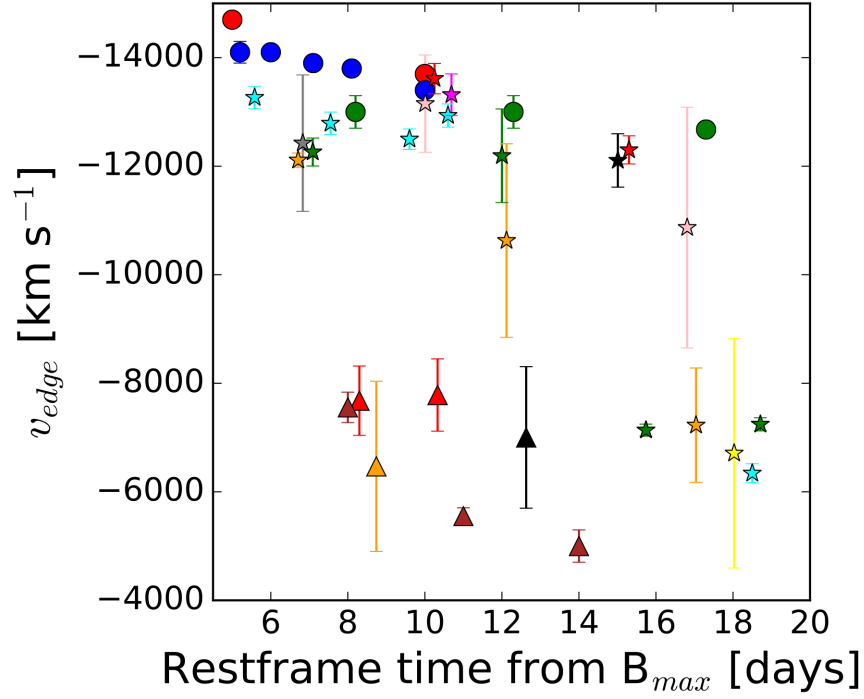
with the appropriate SN name and rest frame time relative to maximum. The figure shows only the H -band region of each spectrum.³

3. TECHNIQUE

Here we describe our method to measure v_{edge} . As demonstrated in Fig. 3, v_{edge} was measured by fitting the minimum of the region blueward of the iron peak emission feature with a Gaussian profile. The fit is weighted by the observational flux uncertainty. The data were fitted over a $\sim 0.05\mu\text{m}$ range around a central value, illustrated by the red lines in Fig. 3. The continuum is defined as a straight line connecting the end points in this range and removed before the fit. The Gaussian fit was iterated, using the previous minimum of the Gaussian as the central point in the new fit, until convergence was met. This was done to ensure the continuum was properly removed. Convergence usually required ~ 5 iterations. We also fit the data with a Mofat function. Using the Bayesian information criterion, and Akaike information criterion, it was found that a Gaussian function models the profile better than a Mofat function.

³ The entire NIR wavelength range of these data will be presented in a future publication.

An accompanying uncertainty to our best-fit value of v_{edge} was determined by producing 100 realizations on a smoothed spectrum with noise added in at each pixel using a normal distribution with the standard deviation of the Gaussian matching the observed flux error, denoted by the light grey error region in the left panel of Figure 3. The flux errors of the FIRE spectra come from the standard deviation in flux of the multiple exposures necessary in NIR observations (Hsiao et al. 2019). This newly constructed spectrum was then measured over the same region and with the same fitting technique as the observed input spectrum. This was done for each realization to create an array of 100 velocity measurements for the given feature whose standard deviation was taken as the measurement error of v_{edge} . If no error spectrum was available from the observations, an array of values was produced through subtracting the smoothed spectrum and the observations. The absolute value of these subtracted values were smoothed to generate a noise trend. This noise trend was used as a representation of the mean noise on the spectra and sampled back on to the smoothed spectra to produce another realization of the observed spectra. For each of the 100 realizations of the Gaussian fit discussed above, a different amount of noise was sampled from the noise trend back onto the smoothed spectra.



●	ASASSN-14lp	★	SNhunt281	★	PSN-171
●	SN 2014j	★	SN 2011iv	▲	SN 2013aj
●	SN 2011fe	★	PS1-14ra	▲	ASASSN-15ga
★	ASASSN-15aj	★	SN 2011jh	▲	SN 1999by
★	LSQ14ajn	★	iPTF13ebh	▲	SN 2015bo
★	SN 2013aj				

Figure 4. *Top:* v_{edge} as a function of rest frame time from maximum. *Bottom:* The iron-peak outer velocity at $+10 \pm 3$ d as a function of S_{BV} . For some objects the error bars are smaller than the marker sizes. Normal SNe Ia are marked by solid circle symbols, transitional SNe Ia are marked by star circle symbols, and sub-luminous SNe Ia are marked by solid triangle symbols.

The iron-peak emission region is a multiplet of many allowed Fe/Co/Ni lines and not from an individual transition. As a result, the different components are sensitive to density and temperature, hence the ionization and excitation state in the centre of the feature can differ. However, the Doppler shift of the highest energy (bluest edge) component is not sensitive to density and temperature. This is because it is a result of atomic physics. Therefore we use the outer edge of the feature to measure velocities, as this is a stable measurement. In this work we adopt $1.57\mu\text{m}$ as the rest wavelength of the feature. This value was obtained by checking for the strongest lines from non-LTE radiation transport models of normal and sub-luminous SNe Ia (Höflich et al. 2002; Höflich et al. 2017). However, if the rest wavelength of this feature were to be altered, it would just cause a systematic shift in the values and not change the trend.

4. RESULTS

Using the method described above, v_{edge} was measured for each of the NIR spectra, and the results are presented in the top panel of Fig. 4. Inspection of the measurements reveals v_{edge} decreases over time for the majority of objects. The normal-bright ASASSN-14lp exhibits the highest velocities, reaching $-14,700\pm 100\text{ km s}^{-1}$ on +5.2 d and later $-13,700\pm 100\text{ km s}^{-1}$ on +10.0 d. Transitional objects exhibit slightly lower values of v_{edge} , which then decreases rapidly. For example, SN 2011iv (Gall et al. 2018; Ashall et al. 2018) extends from $v_{edge} = -13,200\pm 200\text{ km s}^{-1}$ at +5.6 d down to $-6300\pm 200\text{ km s}^{-1}$ by +10 d. The least luminous SNe Ia have the lowest values of v_{edge} , clustering around $-6,000\text{ km s}^{-1}$. At +8 d SN 1999by has a v_{edge} of $-7,600\pm 300\text{ km s}^{-1}$ and by +14 d it drops to $-5,000\pm 300\text{ km s}^{-1}$.

SNe Ia with a v_{edge} of $\sim -10,000\text{ km s}^{-1}$ appear to be rare. However, SN 2011iv, SN hunt281 and iPTF13ebh are the only objects which rapidly drops over the time period examined. For example, iPTF13ebh exhibits a v_{edge} of $-10,600\pm 1,800\text{ km s}^{-1}$ at +12.12 d, but by +17.04 d it drops to $-7,200\pm 1,000\text{ km s}^{-1}$.

In the bottom panel of Fig. 4, we have plotted v_{edge} as a function of the color-stretch parameter s_{BV} . The points from the spectra at +10 \pm 3 d were plotted because at later times the corresponding layers may become optically thin. Objects exhibiting larger s_{BV} values are found to also exhibit higher values of v_{edge} . v_{edge} was found to range from $\sim -14,000\text{ km s}^{-1}$ for normal-bright SNe Ia, to $-10,500\text{ km s}^{-1}$ for transitional SNe Ia, and down to $\sim -5,000\text{ km s}^{-1}$ for sub-luminous SNe Ia. The correlation between s_{BV} and v_{edge} implies v_{edge} is also

correlated with the peak luminosity of the SNe Ia, and hence the amount of ^{56}Ni produced during the explosion.

From our sample here it is not possible to rule out that there is bimodality in the data, where the sub-luminous SNe Ia have a larger range. However, photometric properties of SNe Ia, such as those from CSP-I show a continuous distribution from normal to sub-luminous SNe Ia (Burns et al. 2018). This implies that the possible bimodal distribution seen in this work is produced by a small sample size, and the fact that transitional SNe Ia are rare. A Pearson correlation test of the points in the bottom panel of Fig. 4 produced a correlation coefficient of -0.86.

5. DISCUSSION

A measure of v_{edge} provides a constraint on of the outer ^{56}Ni distribution in the ejecta. This is due to the fact that the Fe/Co/Ni emission region is located at large radii in the SN atmosphere is an isolated multiplet and is not contaminated by lines from other elements. Furthermore, the highest energy Doppler shift of this region will correspond to the edge of the highest velocity emission, which is a measurement of the outer ^{56}Ni . v_{edge} is therefore an valuable tool to analyze the explosion physics of SNe Ia. For example measuring v_{edge} for a large sample of SNe will probe the mixing of ^{56}Ni in the ejecta.

v_{edge} is a model-independent measurement, and a diagnostic of the location between the complete and incomplete Si-burning regions. It provides an indication of the effectiveness of the burning in the ejecta. Those objects that are brighter, and produce more ^{56}Ni , have experienced more effective burning. The exact details of this will be explored in an accompanying paper with respect to explosion models (Ashall et al. 2019). However, the results here are consistent with those found through nebular phase spectral modeling by Mazzali et al. (1998) who showed that less luminous objects have ^{56}Ni located at lower velocities. A similar result was also found by Botyánszki & Kasen (2017) who demonstrate using nebular phase modeling that a larger ^{56}Ni mass (and therefore SN luminosity) produces broader Fe lines in the ejecta.

Our results indicate that ^{56}Ni is located at lower velocities for less luminous SNe Ia, and may argue against very low mass explosions (less than $\sim 0.9M_{\odot}$) for the sub-luminous SNe Ia. This is because, for the same ^{56}Ni mass, these very low mass explosions tend to have the ^{56}Ni located at higher velocities compared to M_{Ch} explosions (e.g., Sim et al. 2010; Blondin et al. 2018), which may be in contradiction with the values of v_{edge} seen here. Finally, the fact that we see a relatively

smooth distribution in v_{edge} as a function of light curve shape implies that at least some SNe Ia at the faint end of the luminosity width relationship may have a similar explosion mechanism to normal SNe Ia.

We thank many colleagues for fruitful discussions, as well as Josh Simon, Povilas Palunas, and Mansi Kasliwal for providing telescope time. The work presented here has been supported in part by NSF awards AST-1008343 & AST-1613426 (PI: M.M. Phillips), AST-1613472 (PI: E.Y Hsiao), AST-1715133 (PI: P. Hoefflich), AST-16113455 (PI: N. B. Suntzeff) and in part by a Sapere Aude Level II grant (PI: M.D. Stritzinger) from the Danish National Research Foundation (DFF). M.D. Stritzinger and S. Holmbo are generously supported by a research grant (13261) from the VILLUM FONDEN. M.D. Stritzinger and E. Baron acknowledge support from the Aarhus University Research Fund (AUFF) for a Sabbatical research grant. E. Baron acknowledges partial support from NASA Grant NNX16AB25G. Research by D.J. Sand is supported by NSF grants AST-1821967, 1821987, 1813708 and 1813466. We thank the Mitchell Institute for Fundamental Physics and Astronomy for partial support. Based on observations obtained at the Gemini Observatory under program GS-2015A-Q-5 (PI: D. Sand). Gemini is operated by the Association

of Universities for Research in Astronomy, Inc., under a cooperative agreement with the NSF on behalf of the Gemini partnership: the NSF (United States), the National Research Council (Canada), CONICYT (Chile), Ministerio de Ciencia, Tecnología e Innovación Productiva (Argentina), and Ministério da Ciência, Tecnologia e Inovação (Brazil). D. J. Sand is a visiting Astronomer at the Infrared Telescope Facility, which is operated by the University of Hawaii under contract NNH14CK55B with the National Aeronautics and Space Administration. Based in part on observations made with the Nordic Optical Telescope (P49-017, P50-015, and P51-006; PI M.D. Stritzinger), operated by the Nordic Optical Telescope Scientific Association at the Observatorio del Roque de los Muchachos, La Palma, Spain, of the Instituto de Astrofísica de Canarias.

Facilities: Magellan:Baade (FIRE near-infrared echellette), Magellan:Clay (Magellan Inamori Kyocera Echelle), du Pont (Boller & Chivens spectrograph, Gemini:North (GNIRS near-infrared spectrograph), VLT (ISAAC), NTT (EFOSC), IRTF (SpeX near-infrared spectrograph), Hale (DBSP), Hiltner (TIFKAM), NOT (ALFOSC), UH:2.2m (SNIFS), FLWO:1.5m (FAST), HST (STIS), La Silla-QUEST, CRTS, iPTF, ASAS-SN, PS1)

Facilities: Python, IRAF, IDL

Table 1. The properties of the SNe Ia and a log of the NIR and optical spectral observations. The $\Delta m_{15}(B)$ values were obtained from a direct spline fit to the data, and the values of s_{BV} were obtained from the best fits from SNooPy.

SN	z	s_{BV}	$\Delta m_{15}(B)$ mag	T_{Bmax}^{20} JD−2,450,000	T_{spec}^{21} JD−2,450,000	Phase ²² days	v_{edge} km s ^{−1}	Instrument/Telescope
NIR								
ASASSN-14lp	0.005	1.08±0.05	0.85±0.07	57015.3	57020.3	+5.0	−14700±100	F2/Gemini-S
					57025.3	+10.0	−13700±100	F2/Gemini-S
SN 2014J	0.0001	1.05±0.086	1.05±0.05	56689.75	56694.95	+5.2	−14,100±200	Mt Abu ²⁶
					56695.78	+6.0	−14,100±100	Mt Abu ²⁶
					56696.93	+7.1	−13,900±100	Mt Abu ²⁶
					56697.92	+8.1	−13,800±100	Mt Abu ²⁶
					56699.84	+10.0	−13,400±100	Mt Abu ²⁶
SN 2011fe	0.001	0.95±0.01	1.21±0.05	55813.93	55822.13	+8.2	−13,800±600	GNIRS/Gemini-N
					55826.22	+12.3	−13,500±100	GNIRS/Gemini-N
					55831.21	+17.3	−13,300±100	GNIRS/Gemini-N

Table 1 continued

²⁶ Marion et al. (2015)

Table 1 (*continued*)

SN	z	s_{BV}	$\Delta m_{15}(B)$	T_{Bmax}^{23}	T_{spec}^{24}	Phase ²⁵	v_{edge}	Instrument/Telescope
			mag	JD−2,450,000	JD−2,450,000	days	km s ^{−1}	
SN 2011jh	0.008	0.80±0.01	1.46±0.01	55931.06	55941.84	+10.69*	−13,300±400	FIRE/Baade
SN 2013aj	0.009	0.78±0.01	1.47±0.01	56361.37	56371.72	+10.25*	−13,600±300	FIRE/Baade
					56376.81	+15.30*	−12,300±300	FIRE/Baade
PS1-14ra	0.028	0.77±0.01	...	56724.54	56734.84	+10.01*	−13,000±900	FIRE/Baade
					56741.82	+16.81*	−10,900±2200	FIRE/Baade
ASASSN-15aj	0.011	0.76±0.01	1.44±0.02	57035.46	57050.64	+15.01*	−12,100±500	FIRE/Baade
PSN-171 ²⁷	0.020	0.71±0.01	1.54±0.02	57070.43	57088.82	+18.03*	−6,700±2000	FIRE/Baade
SNhunt281 ²⁸	0.004	0.68±0.01	1.56±0.03	57112.67	57119.79	+7.09*	−12,200±300	FIRE/Baade
					57124.72	+12.00*	−12,200±900	FIRE/Baade
					57128.41	+15.74*	−7,100±100	GNIRS/Gemini-N
					57131.28	+18.71*	−7,200±100	Spex/IRTF
LSQ14ajn ²⁹	0.021	0.64±0.01	1.74±0.02	56734.73	56741.70	+6.83*	−12,400±1200	FIRE/Baade
SN 2011iv	0.006	0.64±0.01	1.74±0.01	55906.08	55911.70	+5.58	−13,200±200	FIRE/Baade
					55913.68	+7.55	−12,800±200	FIRE/Baade
					55915.7	+9.60	−12,500±200	SOFI/NTT
					55916.75	+10.60	−12,900±200	FIRE/Baade
					55924.6	+18.50	−6,300±200	ISAAC/VLT
iPTF13ebh	0.013	0.61±0.01	1.76±0.02	56623.29	56630.0	+6.71	−12,100±100	GNIRS/Gemini-N
					56635.58	+12.12	−10,600±1800	FIRE/Baade
					56640.56	+17.04	−7,200±1000	FIRE/Baade
ASASSN-15ga	0.007	0.50±0.03	2.13±0.04	57115.88	57124.68	+8.74*	−6,500±1500	FIRE/Baade
SN 2015bo	0.016	0.47±0.01	1.85±0.02	57076.02	57088.86	+12.63*	−7,000±1300	FIRE/Baade
SN 2013ay	0.016	0.46±0.05	...	56375.41	56383.84	+8.30*	−7,700±600	FIRE/Baade
					56385.91	+10.33*	−7,800±700	FIRE/Baade
SN 1999by	0.002	0.44±0.01	1.90±0.05	51308	51316	+8	−7,600±300	TIFKAM/Hiltner ³⁰
					51319	+11	−5,500±200	TIFKAM/Hiltner
					51322	+14	−5,000±300	TIFKAM/Hiltner
Optical								
ASASSN-14lp	0.005	1.08±0.05	0.85±0.07	57015.3	57011	−4	...	FLWO-1.5m / FAST ³¹
SN 2014J	0.0001	1.05±0.086	1.05±0.05	56689.75	56692	+2	...	Frodospec/LT ³²
SN 2011fe	0.001	0.95±0.01	1.21±0.05	55813.93	55814	+0	...	SNIFS/UH 2.2m ³³
SN 2011jh	0.008	0.80±0.01	1.46±0.01	55931.06	55927	−4	...	B&C/Du Pont ³⁴
SN 2013aj	0.009	0.78±0.01	1.47±0.01	56361.37	56356	−5	...	EFOSC/NTT ³⁵
PS1-14ra	0.028	0.77±0.01	...	56724.54	56728	+3	...	ALFOSC/NOT ³⁴
ASASSN-15aj	0.011	0.76±0.01	1.44±0.02	57035.46	57035	+0	...	MIKE Clay ³⁴

Table 1 continued

²⁷ J13471211-2422171

²⁸ SN 2015bp

²⁹ SN 2014ah

³⁰ Höflich et al. (2002)

³¹ Shappee et al. (2016)

³² Ashall et al. (2014)

³³ Pereira et al. (2013)

³⁴ Morrell et al. in prep.

³⁵ Smartt et al. (2015)

Table 1 (*continued*)

SN	z	s_{BV}	$\Delta m_{15}(B)$	T_{Bmax}^{23}	T_{spec}^{24}	Phase ²⁵	v_{edge}	Instrument/Telescope
			mag	JD−2,450,000	JD−2,450,000	days	km s ^{−1}	
PSN-171 ²⁷	0.020	0.71±0.01	1.54±0.02	57070.43	57068	−2	...	ALFOSC/NOT ³⁴
SNhunt281 ²⁸	0.004	0.68±0.01	1.56±0.03	57112.67	57108	−5	...	ALFOSC/NOT ³⁴
LSQ14aj ²⁹	0.021	0.64±0.01	1.74±0.02	56734.73	56729	−6	...	ALFOSC/NOT ³⁴
SN 2011iv	0.006	0.64±0.01	1.74±0.01	55906.08	55907	+1	...	STIS/HST ³⁶
iPTF13ebh	0.013	0.61±0.01	1.76±0.02	56623.29	56623	+0	...	DBSP/Palomar200 ³⁷
ASASSN-15ga	0.007	0.50±0.03	2.13±0.04	57115.88	57121	+5	...	ALFOSC/NOT ³⁴
SN 2015bo	0.016	0.47±0.01	1.85±0.02	57076.02	57079	+3	...	B&C/Du Pont ³⁴
SN 1999by	0.002	0.44±0.01	1.90±0.05	51308	51303	−5	...	FAST/FLWO ³⁸

REFERENCES

- Arnett, W. D. 1982, *ApJ*, 253, 785
- Ashall, C., Mazzali, P., Bersier, D., et al. 2014, *MNRAS*, 445, 4427
- Ashall, C., Mazzali, P., Sasdelli, M., & Prentice, S. J. 2016, *MNRAS*, 460, 3529
- Ashall, C., Mazzali, P. A., Pian, E., & James, P. A. 2016, *MNRAS*, 463, 1891
- Ashall, C., Mazzali, P. A., Stritzinger, M. D., et al. 2018, *MNRAS*, 477, 153
- Ashall, C., Hoefflich, P., Hsiao, E. Y., et al. 2019, *arXiv:1904.01633*
- Avelino, A., Friedman, A. S., Mandel, K. S., et al. 2019, *arXiv:1902.03261*
- Blondin, S., Dessart, L., & Hillier, D. J. 2018, *MNRAS*, 474, 3931
- Blondin, S., Dessart, L., Hillier, D. J., & Khokhlov, A. M. 2017, *MNRAS*, 470, 157
- Botyánszki, J., & Kasen, D. 2017, *ApJ*, 845, 176
- Burns, C. R., Stritzinger, M., Phillips, M. M., et al. 2014, *ApJ*, 789, 32
- Burns, C. R., Parent, E., Phillips, M. M., et al. 2018, *ApJ*, 869, 56
- Dhawan, S., Leibundgut, B., Spyromilio, J., & Blondin, S. 2017, *A&A*, 602, A118
- Dhawan, S., Jha, S. W., & Leibundgut, B. 2018, *A&A*, 609, A72
- Filippenko, A. V., Richmond, M. W., Branch, D., et al. 1992, *AJ*, 104, 1543
- Gall, C., Stritzinger, M. D., Ashall, C., et al. 2018, *A&A*, 611, A58
- Garnavich, P. M., Bonanos, A. Z., Krisciunas, K., et al. 2004, *ApJ*, 613, 1120
- Hoefflich, P., Hsiao, E. Y., Ashall, C., et al. 2017, *ApJ*, 846, 58
- Höflich, P., Gerardy, C. L., Fesen, R. A., & Sakai, S. 2002, *ApJ*, 568, 791
- Hsiao, E. Y., Phillips, M. M., Marion, G. H., et al. 2019, *PASP*, 131, 014002
- Hsiao, E. Y., Burns, C. R., Contreras, C., et al. 2015, *A&A*, 578, A9
- Hsiao, E. Y., Marion, G. H., Phillips, M. M., et al. 2013, *ApJ*, 766, 72
- Hsiao, E. Y., Marion, G. H., Morrell, N., et al. 2013, *The Astronomer’s Telegram*, 4935,
- Hsiao, Y. C. E. 2009, Ph.D. Thesis,
- Iben, I., Jr., & Tutukov, A. V. 1984, *ApJS*, 54, 335
- Kattner, S., Leonard, D. C., Burns, C. R., et al. 2012, *PASP*, 124, 114
- Kirshner, R. P., Willner, S. P., Becklin, E. E., Neugebauer, G., & Oke, J. B. 1973, *ApJL*, 180, L97
- Krisciunas, K., Suntzeff, N. B., Phillips, M. M., et al. 2004, *AJ*, 128, 3034
- Livio, M., & Mazzali, P. 2018, *PhR*, 736, 1
- Livne, E. 1990, *ApJL*, 354, L53
- Marion, G. H., Höflich, P., Gerardy, C. L., et al. 2009, *AJ*, 138, 727
- Marion, G. H., Sand, D. J., Hsiao, E. Y., et al. 2015, *ApJ*, 798, 39

³⁶ Gall et al. (2018)³⁷ Hsiao et al. (2015)³⁸ Garnavich et al. (2004)

- Mandel, K. S., Narayan, G., & Kirshner, R. P. 2011, *ApJ*, 731, 120
- Mazzali, P. A., Cappellaro, E., Danziger, I. J., Turatto, M., & Benetti, S. 1998, *ApJL*, 499, L49
- Mazzali, P. A., Röpke, F. K., Benetti, S., & Hillebrandt, W. 2007, *Science*, 315, 825
- Pastorello, A., Mazzali, P. A., Pignata, G., et al. 2007, *MNRAS*, 377, 1531
- Pereira, R., Thomas, R. C., Aldering, G., et al. 2013, *A&A*, 554, A27
- Phillips, M. M. 1993, *ApJL*, 413, L105
- Phillips, M. M. 2012, *PASA*, 29, 434
- Phillips, M. M., Contreras, C., Hsiao, E. Y., et al. 2019, *PASP*, 131, 014001
- Riess, A. G., Macri, L. M., Hoffmann, S. L., et al. 2016, *ApJ*, 826, 56
- Scalzo, R. A., Parent, E., Burns, C., et al. 2019, *MNRAS*, 483, 628
- Sim, S. A., Röpke, F. K., Hillebrandt, W., et al. 2010, *ApJL*, 714, L52
- Shappee, B. J., Piro, A. L., Holoiien, T. W.-S., et al. 2016, *ApJ*, 826, 144
- Smartt, S. J., Valenti, S., Fraser, M., et al. 2015, *A&A*, 579, A40
- Stritzinger, M., Mazzali, P. A., Sollerman, J., & Benetti, S. 2006, *A&A*, 460, 793
- Wheeler, J. C., Höflich, P., Harkness, R. P., & Spyromilio, J. 1998, *ApJ*, 496, 908
- Whelan, J., & Iben, I., Jr. 1973, *ApJ*, 186, 1007
- Wood-Vasey, W. M., Friedman, A. S., Bloom, J. S., et al. 2008, *ApJ*, 689, 377
- Yaron, O., & Gal-Yam, A. 2012, *PASP*, 124, 668